Materials Advances

ROYAL SOCIETY OF CHEMISTRY

PAPER

View Article Online
View Journal | View Issue

Cite this: *Mater. Adv.*, 2025, 6, 3716

Oxygen vacancies induced low overpotentials of Ag/CeO_2 for electrocatalytic evolution of oxygen and hydrogen†

Ajit Kumar Dhanka,[a] Mayank Tiwari,[b] Prashant Kumar Bhartiya,[c] Balaram Pani,[d] Nityananda Agasti *[a] and Debabrata Mishra *[b]

Designing efficient catalysts for the evolution of hydrogen and oxygen through electrocatalytic water splitting remains an area of significant interest. Herein, we develop an Ag/CeO_2 catalyst that demonstrates a remarkable electrocatalytic performance for hydrogen and oxygen evolution through water splitting. The high catalytic activity can be attributed to the interaction between Ag and CeO_2, which increases the oxygen vacancies at the interface. This is substantiated by the results from Raman, X-ray photoelectron, electron paramagnetic resonance and photoluminescence spectroscopy. The reduced photoluminescence intensity validates the effective separation of photogenerated electron–hole pairs due to oxygen vacancies. Besides increasing the oxygen vacancies, Ag enhances light absorption and reduces the band gap of CeO_2, which is evident from a remarkable enhancement in the electrocatalytic activity of Ag/CeO_2, especially under light illumination, compared to pristine CeO_2. Notably, a drastic reduction in overpotential and an increase in current density are observed for Ag/CeO_2. For the oxygen evolution reaction, Ag/CeO_2 exhibits a reduction of 120 mV in the overpotential and an increase of 19.8 mA cm^{-2} in the current density with the lowest Tafel slope of 158 mV dec^{-1} compared to CeO_2. For the hydrogen evolution reaction, Ag/CeO_2 exhibits a reduction of 130 mV in the overpotential and an increase of 14.1 mA cm^{-2} in the current density. Considering the results from characterization techniques and electrocatalytic experiments, a plausible mechanism has been proposed for the electrocatalytic performance of the catalyst. This study offers insights into defect-induced ceria-based materials for optimizing and designing effective electrocatalysts for overall water splitting.

Received 3rd April 2025,
Accepted 21st April 2025

DOI: 10.1039/d5ma00321k

rsc.li/materials-advances

1. Introduction

Fossil fuels such as coal, natural gas, and crude oil are essential for meeting energy demands and are used to power various aspects of daily life, agriculture, transportation, and industry. However, the excessive consumption of fossil fuels, due to the combination of rapid economic expansion and an increasing global population, presents a significant threat of future shortages.[1] Researchers have predicted that the crude oil may be depleted in 40–50 years,[2] coal production will peak by 2042–2062,[3] and demand for clean energy is projected to rise 50% by 2030.[4] To address these challenges, hydrogen emerges as a viable solution, offering a clean, efficient energy alternative with high energy density and zero carbon emissions.[5,6] Steam reforming is a cost-effective way to produce hydrogen; however, it has environmental limitations.[7] In contrast, electrochemical water splitting offers a cleaner and more sustainable method for generating hydrogen. Electrochemical water splitting consists of the hydrogen evolution reaction (HER) to produce hydrogen and the oxygen evolution reaction (OER) to generate oxygen.[8] High overpotentials, sluggish reaction kinetics, catalyst stability, and the requirement for scalable, inexpensive materials are some of the challenges faced by HER and OER electrocatalysts.[9,10] Electrocatalytic water splitting using semiconductor metal oxides as catalysts has gained significant interest.[11,12] Oxides of rare earth metals, especially cerium (Ce), have been widely used as catalysts due to their flexible interconversion of the oxidation state (Ce^{4+} ↔ Ce^{3+}). The conversion

[a] *Department of Chemistry, University of Delhi, North Campus, Delhi, 110007, India. E-mail: nnagasti@chemistry.du.ac.in*
[b] *Department of Physics and Astrophysics, University of Delhi, Delhi, 110007, India*
[c] *Delhi School of Climate Change and Sustainability, Institution of Eminence (IOE), University of Delhi, Delhi, 110007, India*
[d] *Department of Chemistry, Bhashkaracharya College of Applied Sciences, University of Delhi, Dwarka, New Delhi, 110075, India*

† Electronic supplementary information (ESI) available: UV-vis spectra, calculated band gaps by UV-vis diffuse reflectance spectroscopy (DRS), XRD peak broadening, Raman peak shifting, XPS spectra with the calculated area of Ce 3d peaks for CeO_2 and Ag/CeO_2 nanocomposites, low resolution TEM image, calculated average size, and electrochemical impedance spectroscopy (EIS). See DOI: https://doi.org/10.1039/d5ma00321k

between Ce^{4+} and Ce^{3+} results in the formation of oxygen vacancies in the lattice structure denoted as Ce^{4+}–O_v–Ce^{3+} (where O_v represents an oxygen vacancy), an inherent property of CeO_2 that makes it a potential redox material for electrocatalytic oxygen evolution reactions (OER).[13,14] Moreover, CeO_2, being an n-type semiconductor with a band gap of 3.2 eV, acts as a good photocatalyst.[15] Its remarkable redox behavior and suitable band gap make it a potential candidate for photoelectrocatalysis. However, there are limitations with ceria due to its wide band gap. Therefore, it is of great importance to develop highly efficient ceria nanostructures for photoelectrocatalytic applications.

Recently, the development of ceria-based nanomaterials by modulating the band gap and increasing defects on the ceria surface has been demonstrated as an effective strategy to improve the light-harvesting capability and restrain electron–hole recombination for enhanced photoelectrocatalytic performance.[16–18] For example, Ghosh *et al.* have reported a ceria-based heterojunction catalyst for hydrogen evolution, where the band gap and defects in ceria contributed to enhanced photoelectrocatalytic activity.[19] Although efforts were made to prepare ceria-based materials, reports on in-depth characterization of defects in ceria and the mechanistic details highlighting the role of defects in the catalytic performance of the material are limited.[20–23] Hence, this work offers a detailed study revealing structural characterization of defects in ceria-based materials and a mechanistic study of the roles of defects in catalytic activity. Besides having good catalytic properties, ceria also acts as a good catalyst support, onto which metal or metal oxide nanoparticles can be incorporated to produce heterojunctions. The introduction of metal nanoparticles onto the surface of a ceria support forms metal–ceria junctions, which can result in a synergistic effect and facilitate interfacial charge transfer, thereby improving photoelectrocatalytic performance. Furthermore, the metal nanoparticles can act as photosensitizers to strengthen the light absorption of the metal–ceria composite. Additionally, the strong metal–support interaction between metal nanoparticles and ceria increases defects on the surface of ceria and reduces the band gap in ceria.

Considering the importance of developing high-performance electrocatalysts based on ceria-based materials, in this report we describe Ag/CeO_2 prepared by a solvothermal method, as an effective catalyst for oxygen and hydrogen evolution by electrocatalytic water splitting. The electrocatalytic performance of Ag/CeO_2 as a catalyst is found to be distinctly higher than that of pristine CeO_2 for electrocatalytic water splitting. The activity of Ag/CeO_2 was enhanced remarkably under light illumination. Ag/CeO_2 exhibited a 120 mV reduction in the overpotential and a 19.8 mA cm^{-2} increase in the current density compared to CeO_2 for the oxygen evolution reaction. For the hydrogen evolution reaction, Ag/CeO_2 exhibited superior activity to CeO_2 with an overpotential reduction of 130 mV and a 14.1 mA cm^{-2} enhancement in the current density. The materials characterization results confirm the role of Ag and Ag/CeO_2 (metal–support) interactions in achieving enhanced electrocatalytic performance. Ag nanoparticles improve light absorption and enhance the absorption intensity through the localized surface plasmon resonance (LSPR) effect at the Ag/CeO_2 interface. The incorporation of Ag also reduces the band gap of CeO_2 to 2.90 eV. Moreover, due to the strong metal–support interaction between Ag and CeO_2, there is an increase in surface oxygen vacancies on CeO_2. The surface oxygen vacancies trap the photogenerated electrons causing delayed recombination of photogenerated electron and hole pairs. Overall, the interaction between Ag and CeO_2 improves the optical properties, reduces the band gap, enhances the charge carrier separation, and restrains the recombination of photogenerated carriers, thereby resulting in an improvement in the overall water splitting process. A plausible mechanism was also proposed to understand the role of the Ag/CeO_2 catalyst in electrocatalytic water splitting for hydrogen and oxygen evolution reactions.

2. Experimental section

2.1 Materials

Cerium nitrate hexahydrate (99%) ($Ce(NO_3)_3{\cdot}6H_2O$) and sodium hydroxide (98%) (NaOH) were obtained from CDH India; silver nitrate ($AgNO_3$, 98.5%) from Merck; and ethanol (C_2H_5OH) and methanol (CH_3OH) from Sigma-Aldrich, India. Deionized (DI) water was used in the experiments. All chemicals used were of analytical grade and directly used as received without further purification. Ag/CeO_2 nanocomposites were synthesized following the literature method.[24]

2.2 Preparation of Ag/CeO_2

The Ag/CeO_2 nanocomposites were prepared *via* a solvothermal method[24,25] (Scheme 1). In a typical synthesis procedure, a 1 : 10 weight ratio of $AgNO_3$ to $Ce(NO_3)_3{\cdot}6H_2O$, corresponding to a molar ratio of $AgNO_3$ (0.59 mmol) to $Ce(NO_3)_3$ (2.4 mmol), was used. Firstly, 0.1 g of $AgNO_3$ and 1.0 g of $Ce(NO_3)_3{\cdot}6H_2O$ were dissolved in 50 mL of methanol, followed by the addition of 0.25 g (6.25 mmol) of sodium hydroxide under magnetic stirring for 30 minutes to create a homogenous solution. Furthermore, the resultant reaction mixture was transferred to a 100 ml Teflon-lined stainless-steel autoclave and sealed. Then, the autoclave was heated at 180 °C and maintained at this temperature for 18 hours. The autoclave was left to cool naturally to room temperature. The formed precipitate was collected and washed three to four times with ethanol by centrifugation at 3000 rpm for 10 minutes to remove any residual chemicals from the precipitate. Afterward, the precipitate was heated in an oven at 80 °C for 4 hours and subsequently calcined at 250 °C for 2 hours, yielding a grey color powder of Ag/CeO_2 nanocomposites. For comparison, CeO_2 nanoparticles were synthesized using a similar procedure but without the addition of $AgNO_3$. No additional reducing agent was used in the preparation of materials. In the presence of NaOH, $Ce(NO_3)_3{\cdot}6H_2O$ precipitates into $Ce(OH)_3$, which under hydrothermal conditions converts into CeO_2. $AgNO_3$ in the presence of NaOH forms Ag_2O as an intermediate to form Ag

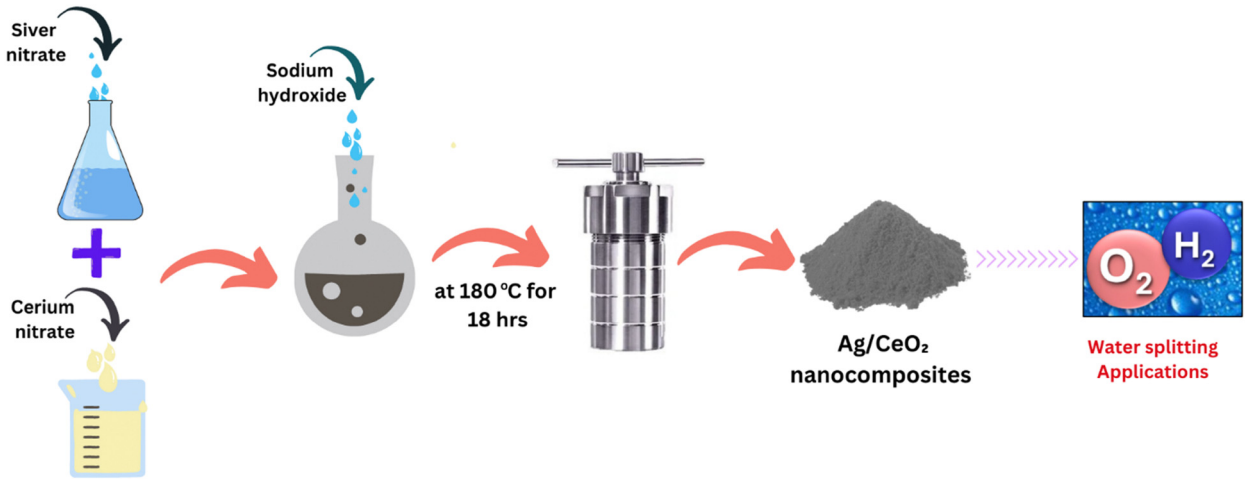

Scheme 1 Preparation of Ag/CeO_2 nanocomposites by a solvothermal method and their application in water splitting.

nanoparticles. NaOH facilitates the nucleation of Ag nanoparticles.[26]

2.3 Fabrication of electrodes for electrochemical measurements

The electrodes were fabricated by drop-casting the prepared CeO_2 and Ag/CeO_2 on nickel foam (NiF). The first electrode was fabricated by drop-casting CeO_2 as the active material, polyvinylidene fluoride (PVDF) as the binder, and carbon black as the conducting agent. The ratio of these components was 75 : 15 : 10, respectively. Similarly, the second electrode was prepared by drop-casting Ag/CeO_2 as the active material, PVDF as the binder, and carbon black as the conducting agent in the same ratio. These composites were applied onto a nickel foam using the drop-casting method, covering an area of 1 cm^2. Following the application of the coating, the electrodes were placed in a vacuum oven at a temperature of 80 °C for 10 hours to facilitate drying. Subsequently, the electrodes were allowed to cool down naturally until they reached room temperature. The fabricated electrodes were named NiF, NiF/CeO_2, and $NiF/Ag/CeO_2$. NiF/CeO_2/Light and $NiF/Ag/CeO_2$/Light have been abbreviated to the electrocatalytic activity of NiF/CeO_2 and $NiF/Ag/CeO_2$ under light illumination.

2.4 Electrochemical measurements

Electrochemical measurements including linear sweep voltammetry (LSV), electrochemical impedance spectroscopy (EIS), and chronoamperometry were conducted in an alkaline environment using a computerized potentiostat/galvanostat (CS350 Corr-Test electrochemical workstation) within a standard three-electrode electrochemical setup. The counter electrode used was platinum (Pt) and Ag/AgCl was utilized as the reference electrode. The potential values were converted to the reversible hydrogen electrode (E_{RHE}) scale using the Nernst equation.[27] All the electrochemical experiments were conducted using a 1 M KOH solution as the electrolyte. The visible light source emitting a wavelength of λ = 405 nm was utilized for illumination during the electrochemical experiments, which was positioned 5 cm away from the working electrode.

2.5 Materials characterization

The microstructural and morphological features of the synthesized materials were characterized by multiple techniques. Powder X-ray diffraction (PXRD) was conducted to study the crystalline patterns of the materials using a diffractometer with Cu K radiation (λ = 0.1542 nm) in the 2θ range of 10–80. To study the optical properties of the materials, UV-visible spectra were obtained using a Shimadzu 1800 spectrometer and UV-vis diffuse reflectance spectra (DRS) were obtained using an Agilent Cary 5000. Raman spectroscopy study was carried out using a laser Raman spectrometer, model: inVia II. Field emission scanning electron microscopy (FESEM) using an Oxford-EDX system IE 250 X Max 80 (FEI Quanta 200 F SEM) at a high-resolution with a thermally aided field emission gun (FEG) at an acceleration voltage of U_{acc} = 0.2−30 kV was conducted to study the morphology and elemental composition of the materials. High-resolution transmission electron microscopy (HRTEM) images of the materials were collected using a TECNAI G20 HR-TEM 200 kV. To assess the surface area and pore characteristics of the synthesized materials, nitrogen adsorption–desorption measurements were carried out using the Autosorb-iQ XR system from Quantachrome Instruments. Prior to analysis, the samples were degassed at 150 °C for 10 hours under a high vacuum of approximately 1 × 10^{-2} bar to remove any adsorbed impurities. The isotherms were subsequently recorded at 77 K, employing a liquid nitrogen environment to ensure accurate measurements. X-ray photoelectron spectroscopy (XPS) was performed using a Kratos Axis Supra Plus XPS equipped with a monochromatic Al Kα X-ray source (1486.6 eV). The high-resolution data were calibrated using the C 1s peak at a binding energy of 284.5 eV as the standard. The photoluminescence (PL) study was performed at normal temperature on a Horiba Yvon PTI Quanta-Master (8450–11) spectrophotometer with a 375 nm nano-LED as the excitation source. The charge carrier lifetimes were

determined by employing time-resolved photoluminescence (TRPL) measurements (in micro- and milliseconds) using a 980 nm laser and a xenon lamp as light sources in modulated mode.

3. Results and discussion

3.1 Structure, morphology, and elemental analysis

To understand the formation of the Ag/CeO_2 nanocomposite, the optical properties were analyzed by UV-visible spectroscopy and compared with those of pristine CeO_2. The absorption bands at wavelengths of 340 nm and 327 nm in the UV-visible absorption spectra (Fig. S1, ESI†) correspond to Ag/CeO_2 and CeO_2, respectively.[28] The absorption band corresponding to Ag/CeO_2 suffers a red shift compared to CeO_2. The red shift in the absorption band can be attributed to a decrease in the band gap of Ag/CeO_2 because of the addition of Ag, suggesting the formation of the composite material.[29] To calculate the direct band gap energy (E_g) of Ag/CeO_2, UV-vis diffuse reflectance spectra (DRS) were recorded. To mitigate the influence of scattered light, the DRS spectra were transformed using the Kubelka–Munk (K–M) function. The plot of the K–M function *versus* the energy of light is shown in Fig. S2 (ESI†). From this plot, the band gap energies for Ag/CeO_2 were derived. The intercept on the abscissa axis of a linear fit of the Kubelka–Munk function $\alpha h\nu = A(h\nu - E_g)^{n/2}$ corresponds to the E_g values, where E_g, α, A, h, and ν represent the band gap, absorption coefficient, a constant, Planck's constant, and light frequency, respectively.[30] The DRS spectra reveal band gap energies of 3.25 eV for CeO_2 and 2.90 eV for Ag/CeO_2, which represent the energy gap between the valence band and conduction band. The reduction in band gap and the shift of the absorption band to a longer wavelength in Ag/CeO_2 are attributed to the incorporation of Ag into CeO_2 because the addition of Ag facilitates the excitation of electrons from the conduction band to the valence band within the CeO_2 lattice.[31] The formation of Ag/CeO_2 was confirmed by XRD analysis in the 2θ range of 10–80°. The XRD pattern (Fig. 1a) for pristine CeO_2 exhibited peaks at 2θ angles of 28.4°, 32.9°, 47.5°, 56.3°, 59.0°, 69.3°, 76.7°, and 78.8°, corresponding to the (111), (200), (220), (311), (222), (400), (331), and (420) planes, respectively. These peaks are indicative of a cubic fluorite structure, consistent with the JCPDS File No. 34-0394.[32] Compared to pristine CeO_2, the XRD pattern of Ag/CeO_2 exhibits additional peaks at 38.5°, 47.7°, 64.9°, and 76.7° corresponding to the (111), (200), (220), and (311) planes of cubic Ag (peaks presented with asterisks)[33,34] (JCPDS No. 04-0783). The appearance of these peaks confirms the successful incorporation of Ag into CeO_2. This incorporation is further supported by a shift in diffraction peaks to higher angles in Ag/CeO_2 compared to pristine CeO_2, as shown in Fig. S3 (ESI†). This shift is most noticeable in the prominent (111) diffraction peak of Ag/CeO_2.[35,36] Additionally, in the diffraction pattern of Ag/CeO_2, there is a decrease in the intensity and broadening (Fig. S3, ESI†) of all diffraction peaks corresponding to CeO_2, suggesting defect generation in CeO_2 due to Ag addition.[37] The broadening of peaks can be attributed to the reduction in the crystallite size of CeO_2. The average crystallite size, calculated using the Scherrer equation[38] ($D = K\lambda/\beta\cos\theta$ with $K = 0.98$, $\lambda = 1.54$ Å, and β being the full width at half maximum (FWHM) of the (111) peak), was found to be approximately 7 nm for CeO_2 and 6 nm for Ag/CeO_2.

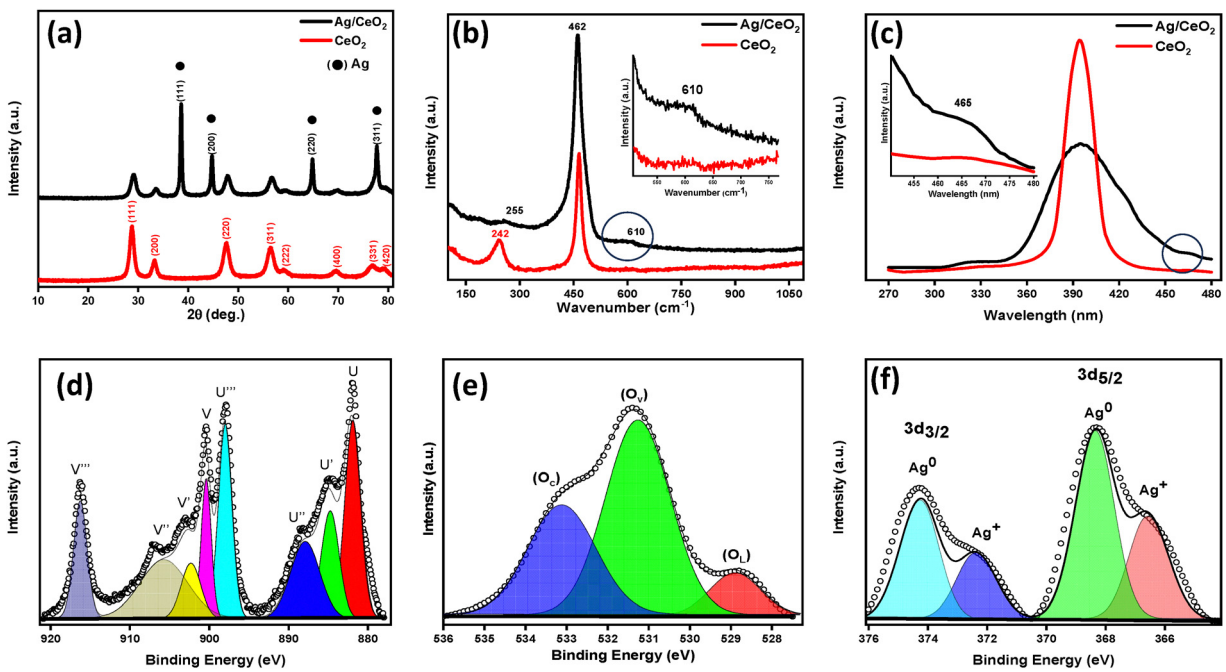

Fig. 1 (a) XRD patterns, (b) Raman spectra, and (c) PL spectra of CeO_2 and Ag/CeO_2 nanocomposites and the XPS spectra and (d) deconvoluted spectra of Ce 3d, (e) O 1s, and (f) Ag 3d for Ag/CeO_2 nanocomposites.

To further support the formation of Ag/CeO_2 nanocomposites and confirm the formation of defects (oxygen vacancies) on the surface of ceria, Raman spectra were recorded in the range of 100–1100 cm^{-1} (Fig. 1b). The prominent peak at 465 cm^{-1} in the spectra corresponds to the F_{2g} mode originating from the symmetric stretching of the Ce–O bond.[39,40] Compared to pristine CeO_2, the Ag/CeO_2 composites exhibited a shift towards a lower wave number in the F_{2g} stretching mode, with a peak at 462 cm^{-1} (Fig. S4a, ESI†). This downshift is due to an increase in oxygen vacancies induced by the incorporation of Ag[41] because oxygen vacancies disrupt the Ce–O vibrational unit leading to the downshift of the F_{2g} mode. In the Ag/CeO_2 composite, additional peaks appearing with distinct intensities at 255 and 610 cm^{-1} correspond to the F_{1u} symmetric mode[42] and the defect-induced mode (*D*) due to intrinsic oxygen vacancies.[43] The band at 610 cm^{-1}, which is not present in pristine CeO_2, shows an increase in oxygen vacancies in Ag/CeO_2. An increase in oxygen vacancies in Ag/CeO_2 is also inferred from the expansion in the FWHM of the F_{2g} peak compared to that of pristine CeO_2[41] (Fig. 1d and Fig. S4a, ESI†). The increase in oxygen vacancies has been calculated from the ratio of the integrated area of the *D* peak to the F_{2g} peak ($I_D/I_{F_{2g}}$), which is a key parameter for measuring the relative concentration of oxygen vacancies on the surfaces of CeO_2 and Ag/CeO_2. The Ag/CeO_2 catalyst demonstrates a higher $I_D/I_{F_{2g}}$ ratio compared to pristine CeO_2, suggesting higher oxygen vacancies in Ag/CeO_2 (Fig. S4b, ESI†). Additionally, the incorporation of Ag in the composite is further confirmed by the enhanced the F_{2g} peak intensity, which arises from the strong optical absorption associated to the surface enhanced Raman scattering (SERS) effect.[44,45]

Furthermore, Ag/CeO_2 has been studied by photoluminescence (PL) analysis, which is a technique to ascertain oxygen vacancies and the efficiency of charge carrier trapping in semiconductor materials.[46] In this study, PL analysis was utilized to investigate the impact of oxygen vacancies on the separation of photogenerated electron–hole pairs in Ag/CeO_2 nanocomposites. In the PL spectra, CeO_2 emissions are often attributed to 4f → VB (valence band) transitions, which are strongly influenced by defects like oxygen vacancies in the material.[47] The PL spectra of CeO_2 and Ag/CeO_2 nanocomposites, shown in Fig. 1c, cover the range from 270 to 480 nm. For CeO_2, a prominent UV emission peak at 394 nm is observed, corresponding to electron transition from the Ce 4f level to the O 2p level.[48] However, with the introduction of Ag, the intensity of this peak decreased substantially along with an additional emission band appearing at 465 nm. The band at 465 nm is mostly associated with the oxygen vacancies with trapped electrons.[49] The reduced photoluminescence intensity in Ag/CeO_2 suggests improved separation of electron–hole pairs due to the presence of oxygen vacancies, highlighting their role in enhancing charge carrier dynamics and overall material performance. This observation aligns well with the findings reported in previous studies.[50]

To further evaluate the formation of oxygen vacancies, oxidation states of Ce, and elemental composition, Ag/CeO_2 was analyzed by X-ray photoelectron spectroscopy (XPS). The XPS spectra of CeO_2 and Ag/CeO_2 were carefully compared to understand the effect of Ag on CeO_2 in the Ag/CeO_2 nanocomposite. The XPS survey spectra (Fig. S5, ESI†) demonstrate the presence of Ce, O and Ag with peaks in the binding energy ranges of 877–922 eV (Ce 3d), 527–536 eV (O 1s), and 364.5–376.1 eV (Ag 3d). The positions of the photoelectron peaks for all the elements are corrected according to the standard carbon (C 1s) peak, which is set at 284.4 eV.

To analyze the oxidation states of cerium in Ag/CeO_2, the high-resolution XPS spectra for Ce 3d were deconvoluted over the binding energy range of 877 to 922 eV (Fig. 1d). The XPS spectra of Ce 3d can be fitted according to eight characteristic peaks located at U (881.9 eV), U′ (884.7 eV), U″ (887.9 eV), U‴ (897.9 eV), V (900.3 eV), V′ (902.3 eV), V″ (905.6 eV), and V‴ (916.2 eV). The peaks U′ and V′ were identified for Ce^{3+}, which are assigned to the oxygen vacancies, and the rest of the peaks V‴, V″, V, U‴, U″, and U correspond to Ce^{4+}.[51] These peaks indicate the presence of both Ce^{3+} and Ce^{4+} electronic states on the surface of CeO_2. Typically, Ce^{4+} is the predominant valence state on the surface of ceria, with a smaller proportion of Ce^{3+}. The presence of Ce^{3+} alongside Ce^{4+} points to oxygen vacancies within the CeO_2 crystals due to their interconversion.[52]

The surface concentration of Ce^{3+} in Ag/CeO_2 can be determined by calculating the peak integral areas of Ce^{3+} and Ce^{4+} using the following formula:[43]

$$\left[Ce^{+3}\right] = \frac{(Ce^{+3})\text{Area}}{\sum (Ce^{+4} + Ce^{+3})\text{Area}} \times 100$$

The Ce^{3+} content was found to be 17.89% in Ag/CeO_2 and 13.92% in CeO_2 (Table S1 and Fig. S6, ESI†). The higher Ce^{3+} content in Ag/CeO_2 compared to pristine CeO_2 is due to interfacial charge transfer induced by the metal–support interaction between Ag and CeO_2. Moreover, the Ce 3d peaks in Ag/CeO_2 are shifted towards high binding energies compared to pristine CeO_2, which might be a consequence of the interfacial electron transfer from Ag to CeO_2 due to the strong interaction between Ag and CeO_2.[53,54] The Ag/CeO_2 interface becomes oxygen vacancy-rich due to this interaction. Additionally, the presence of oxygen vacancies on the surface can be revealed from the XPS spectra for O 1s within the binding energy range of 527 to 536 eV (Fig. 1e). In the deconvoluted XPS spectra for O 1s, the peaks observed at 528.8 eV (O_L), 531.3 eV (O_V), and 533.1 eV (O_C) in Ag/CeO_2 correspond to lattice oxygen (Ce^{4+}–O^{2-}), oxygen vacancies (Ce^{3+}–O^{2-}), and surface chemisorbed hydroxyl groups (–OH), respectively. The peak at 531.3 eV is ascribed to oxygen vacancies.[41] The presence of Ag is also confirmed by the Ag 3d peaks in the XPS spectra (Fig. 1f). The peaks at 368.2 eV and 374.2 eV, attributed to Ag $3d_{5/2}$ and Ag $3d_{3/2}$, respectively, suggest the presence of metallic silver in Ag/CeO_2. Further analysis of these peaks reveals additional peaks at 366.5 eV and 372.3 eV, which are indicative of Ag^+. In a nutshell, the above results confirm the formation of the Ag/CeO_2 nanocomposite and also reveal the oxidation states of

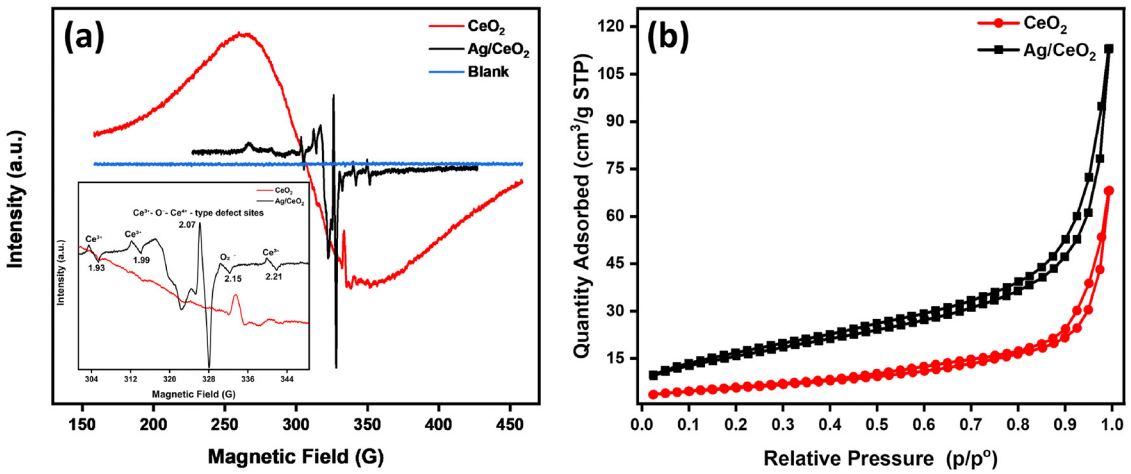

Fig. 2 (a) EPR profiles measured (inset: the calculated *g* factor value) at room temperature and (b) BET analysis for CeO_2 and Ag/CeO_2 nanocomposites.

Ce, the effect of Ag on CeO_2, the interaction between Ag and CeO_2, and oxygen vacancies at the Ag/CeO_2 interface.

The increased oxygen vacancies in Ag/CeO_2 were further validated through electron paramagnetic resonance (EPR) analysis performed at room temperature for both pristine CeO_2 and Ag/CeO_2 samples (Fig. 2a). Compared to pristine CeO_2, Ag/CeO_2 exhibited more pronounced EPR signals, indicating a higher concentration of oxygen vacancies in the composite. The EPR spectra of Ag/CeO_2 revealed distinct *g* values at 1.93, 1.99, and 2.21, which are characteristic of Ce^{3+} ions, thereby confirming the presence of oxygen vacancies. Additionally, signals with *g* values of 2.07 and 2.15 were associated with O^{2-} species and Ce^{3+}–O^{-}–Ce^{4+} defect sites.[55] Collectively, the findings from PXRD, Raman spectroscopy, XPS, and EPR analyses corroborate the enhancement of oxygen vacancies in Ag/CeO_2 compared to pristine CeO_2. This increase in oxygen vacancies is pivotal for the improved electrocatalytic performance of the Ag/CeO_2 composite.

The surface morphology, elemental mapping, and elemental composition of Ag/CeO_2 were characterized by field emission scanning electron microscopy (FESEM) analysis with energy dispersive X-ray analysis (EDX). The FESEM image (Fig. 3a) reveals the spherical shapes of Ag/CeO_2, while the mapping and EDX (Fig. 3b and c) spectrum verify the presence of Ag, Ce, and O with their elemental distributions being 40.44%, 45.68% and 13.89%, respectively.

Furthermore, high-resolution transmission electron microscopy (HRTEM) was employed to investigate the nanostructure of Ag/CeO_2 (Fig. 4a and Fig. S7, ESI†). HRTEM analysis demonstrates Ag nanoparticles deposited onto the CeO_2 surface. The HRTEM image (Fig. 4b) shows Ag (200) and CeO_2 (111) planes with interplanar spacings of 0.205 nm and 0.312 nm, respectively. The corresponding selected area electron diffraction (SAED) patterns (Fig. 4c) reveal the polycrystalline nature of Ag/CeO_2 with resolved lattice fringes indexed to (111), (220), (200), (222), (311), and (420) lattice planes closely matching those obtained from the XRD pattern of Ag/CeO_2 nanocomposites. HRTEM images (Fig. S7, ESI†) reveal that Ag nanoparticles of 4–6 nm size are deposited on CeO_2 particles sized 5–8 nm. The particle sizes are consistent with the crystallite sizes calculated using the Scherrer equation from the XRD pattern. Noticeably, Ag and CeO_2 are in contact with each other, thereby causing defects at the interface. The existence of an interface is crucial as it promotes the increase in surface oxygen vacancies in CeO_2 that can enhance catalysis.

Besides the nanostructure, the specific surface area, pore diameter, and pore volume of the Ag/CeO_2 catalyst have significant effects on its catalytic activities. Therefore, the Brunauer–Emmett–Teller (BET) analysis based on the nitrogen (N_2) adsorption–desorption experiment was conducted. The N_2 adsorption–desorption isotherms (Fig. 2b) show a typical type-IV curve with a fast increase at higher relative pressures (p/p°), indicating the porous structure of the materials.[41] For pristine CeO_2, the BET-specific surface area, total pore volume, and average pore diameter were measured to be 15.88 $m^2\ g^{-1}$, 0.068 $cm^3\ g^{-1}$, and 19.30 nm, respectively. However, in Ag/CeO_2, the surface area properties significantly change to 42.57 $m^2\ g^{-1}$, 1.228 $cm^3\ g^{-1}$, and 11.74 nm, respectively. This noticeable change in structural characteristics is attributed to the introduction of Ag on the CeO_2 surface, which agrees with the results from the previous studies.[56] The porosity and surface area of the material are maintained even after the introduction of Ag.

3.2 Electrochemical measurements (OER and HER)

Oxygen evolution reactions (OER). The electrocatalytic performance of Ag/CeO_2 was evaluated for the oxygen evolution reaction (OER) *via* a three-electrode system in 1 M KOH solution using Ag/AgCl and Pt wire as the reference and counter electrodes, respectively. The working electrodes used were NiF, NiF/CeO_2, NiF/CeO_2/Light, $NiF/Ag/CeO_2$, and $NiF/Ag/CeO_2$/Light. The electrocatalytic performance was studied by linear sweep voltammetry (Table 1). The linear sweep voltammogram (LSV) for the OER performance of NiF, NiF/CeO_2, NiF/CeO_2/Light, $NiF/Ag/CeO_2$, and $NiF/Ag/CeO_2$/Light is shown in Fig. 5a. At a current density of 10 mA cm^{-2}, the overpotentials for NiF, NiF/CeO_2, NiF/CeO_2/Light, $NiF/Ag/CeO_2$, and $NiF/Ag/CeO_2$/

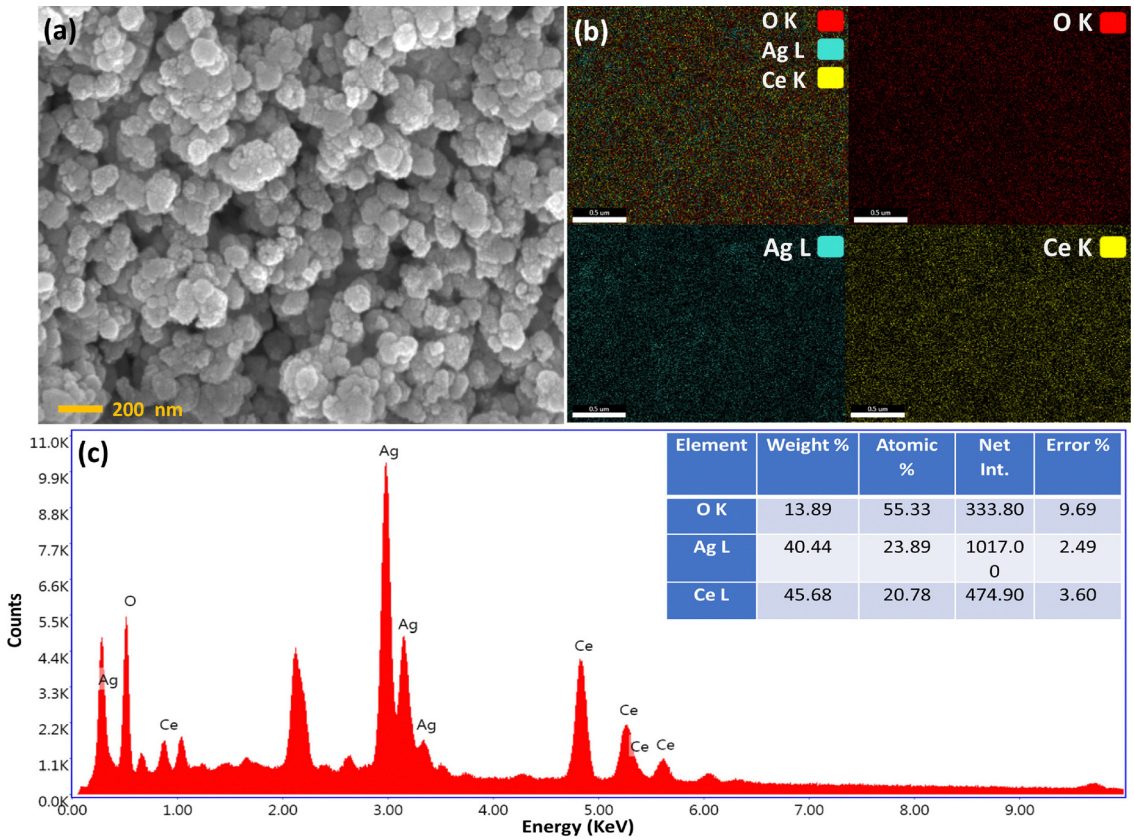

Element	Weight %	Atomic %	Net Int.	Error %
O K	13.89	55.33	333.80	9.69
Ag L	40.44	23.89	1017.00	2.49
Ce L	45.68	20.78	474.90	3.60

Fig. 3 (a) High-magnification FESEM images, (b) EDX elemental mapping, and (c) EDX spectrum of Ag/CeO_2 (inset: atomic and weight percentages of elements present in Ag/CeO_2 nanocomposites).

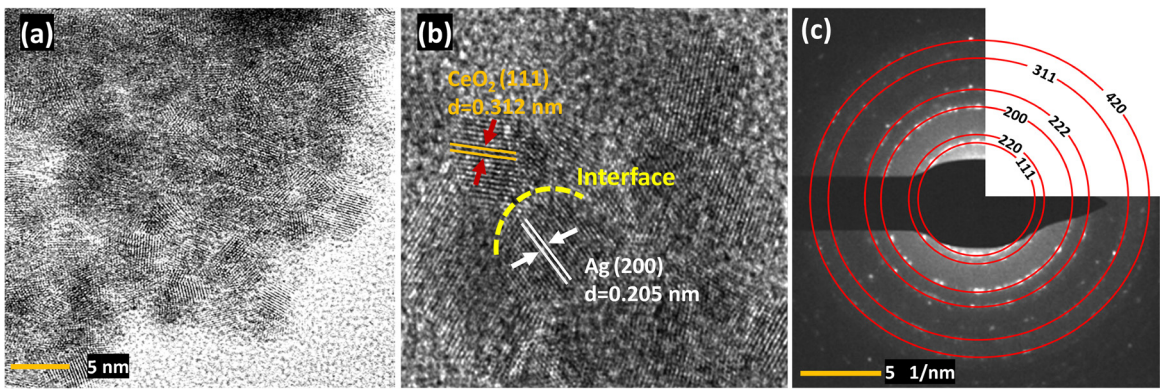

Fig. 4 (a) HRTEM image, (b) interplanar *d*-spacings, and (c) SAED pattern of Ag/CeO_2 nanocomposites.

Light were 730 mV, 620 mV, 560 mV, 500 mV, and 450 mV, respectively (shown in Fig. 5b). Fig. 5c illustrates the current density values for NiF, NiF/CeO_2, NiF/CeO_2/Light, NiF/Ag/CeO_2, and NiF/Ag/CeO_2/Light at a potential of 2.4 V. The corresponding current density values were 29 mA cm^{-2}, 44.6 mA cm^{-2}, 49.9 mA cm^{-2}, 64.4 mA cm^{-2}, and 86.7 mA cm^{-2} (as shown in Fig. 5c). The lower overpotential and high current density signify enhanced OER performance of Ag/CeO_2 deposited on nickel foam (NiF/Ag/CeO_2) compared to CeO_2 on nickel foam (NiF/CeO_2). NiF/Ag/CeO_2 exhibited a 120 mV reduction in the overpotential and a 19.8 mA cm^{-2} increase in the current density compared to NiF/CeO_2. This enhanced performance of NiF/Ag/CeO_2 can be attributed to the improved conductivity facilitated by Ag dispersed on the CeO_2 surface, leading to more efficient charge transfer processes (Fig. S8, ESI†). Furthermore, the overpotential and current density values suggest enhanced electrocatalytic performance of NiF/CeO_2 and NiF/Ag/CeO_2 by illuminating the electrodes with a monochromatic laser light source (λ = 405 nm). This can be attributed to the dispersed Ag boosting the absorption of incident light, which consequently

Table 1 Summary of the OER performance of the electrocatalysts

Oxygen evolution reaction (OER)			
Catalyst	Overpotential at 10 mA cm^{-2} (mV)	Tafel slope (mV dec^{-1})	Current density (mA cm^{-2})
NiF	730	461	29
NiF/CeO_2,	620	273	44.6
NiF/CeO_2/Light	560	241	49.9
NiF/Ag/CeO_2	500	226	64.4
NiF/Ag/CeO_2/Light	450	158	86.7

facilitates the generation of electron–hole pairs in the conduction and valence bands, respectively. Moreover, with the band gap of Ag/CeO_2 being 2.90 eV, the illumination with light of 405 nm wavelength, which is equivalent to ~3.1 eV, facilitates the generation of electron–hole pairs, leading to an enhancement in its OER performance. However, since the band gap of CeO_2 (3.25 eV) is higher than that of Ag/CeO_2 (2.90 eV), the enhancement in the OER under illumination is less pronounced, as shown in Fig. 5a. Under light illumination, the overpotential of NiF/CeO_2 was reduced by 60 mV and the current density increased by 5.3 mA cm^{-2}. Similarly, for NiF/Ag/CeO_2, the overpotential decreased by 50 mV and the current density dramatically increased by 22.3 mA cm^{-2}. Fig. 5d presents the Tafel slopes (OER) for NiF, NiF/CeO_2, NiF/CeO_2/Light, NiF/Ag/CeO_2 and NiF/Ag/CeO_2/Light. The Tafel slope was reduced significantly to 158 mV dec^{-1} for NiF/Ag/CeO_2 in the presence of light, indicating its enhanced OER performance compared to NiF/Ag/CeO_2 with a Tafel slope of 226 mV dec^{-1}, which is attributed to the enhanced reaction kinetics under light illumination and Ag doping. The reaction mechanism for the OER can be given by the following equations:[57]

$$M + OH^- \leftrightharpoons M\text{–}OH + e^-$$

$$M\text{–}OH + OH^- \leftrightharpoons M\text{–}O + H_2O + e^-$$

$$M\text{–}O + OH^- \leftrightharpoons M\text{–}OOH + e^-/2M\text{–}O + OH^- \leftrightharpoons 2M\text{–}O_2 + 2e^-$$

$$M\text{–}OOH + OH^- \leftrightharpoons O_2 + H_2O + e^- + M$$

Here, M represents the active site.

These charge carriers enhance the charge transfer process at the electrode–electrolyte interface, leading to improved reaction kinetics, lower overpotential, and increased current densities.[58,59]

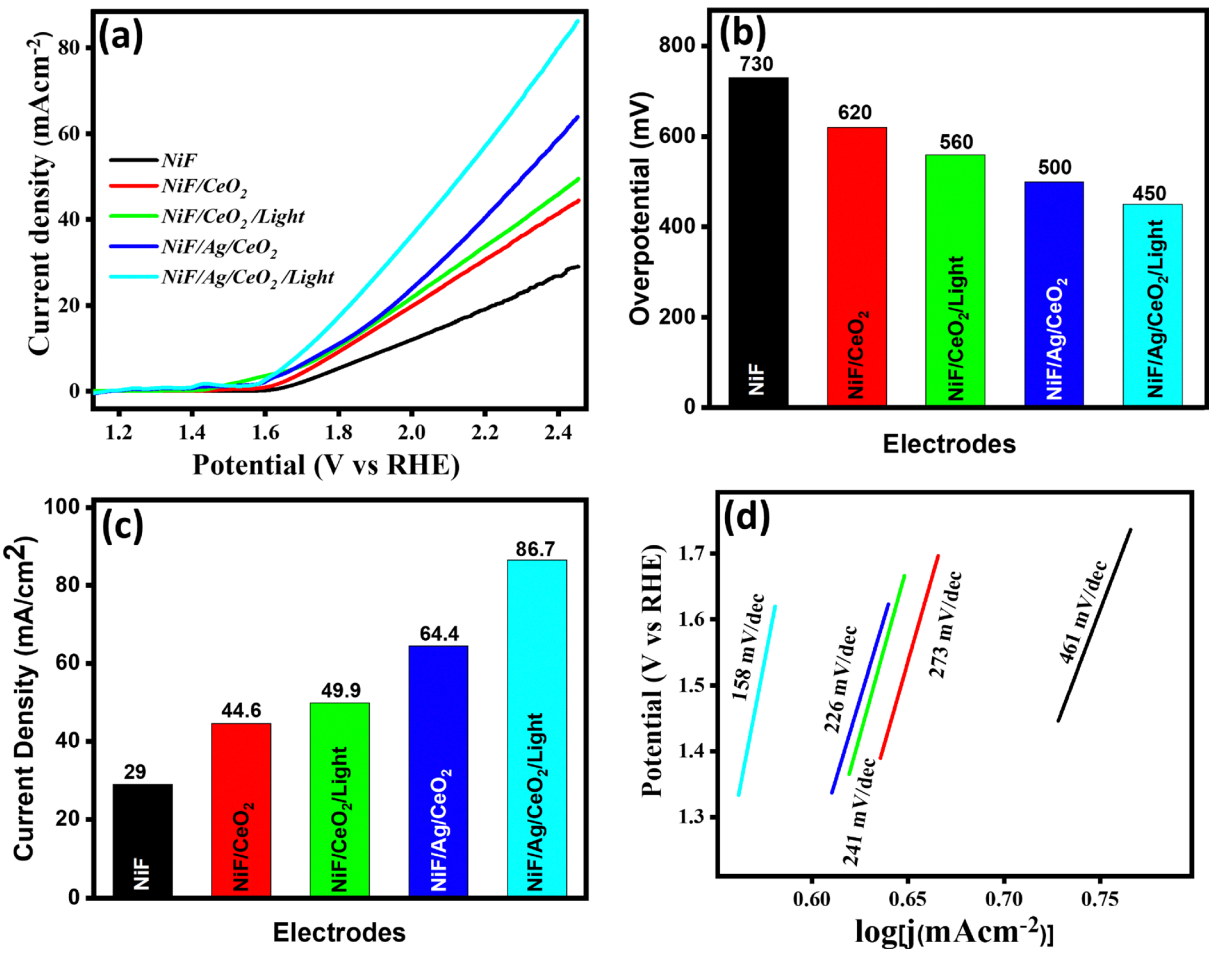

Fig. 5 (a) LSV curves, (b) overpotential (*vs.* RHE) at a current density of 10 mA cm^{-2}, (c) current density at a potential of 2.4 V, and (d) the Tafel slope for the OER of NiF, NiF/CeO_2, NiF/CeO_2/Light, NiF/Ag/CeO_2, and NiF/Ag/CeO_2/Light.

Table 2 Summary of the HER performance of the electrocatalysts

Hydrogen evolution reaction (HER)			
Catalyst	Overpotential at 10 mA cm^{-2} (mV)	Tafel slope (mV dec^{-1})	Current density (mA cm^{-2})
NiF	530	461	10.9
NiF/CeO_2,	410	238	21.2
NiF/CeO_2/Light	330	219	25.3
NiF/Ag/CeO_2	280	169	35.3
NiF/Ag/CeO_2/Light	240	151	45.7

After investigating the OER performance, the electrocatalytic activity for the hydrogen evolution reaction (HER) of the electrodes, including NiF, NiF/CeO_2, NiF/CeO_2/Light, NiF/Ag/CeO_2, and NiF/Ag/CeO_2/Light, was also examined (Table 2). The LSV curves for the HER performance of NiF, NiF/CeO_2, NiF/CeO_2/Light, NiF/Ag/CeO_2, and NiF/Ag/CeO_2/Light are shown in Fig. 6a. The overpotentials calculated at a current density of −10 mA cm^{-2} for NiF, NiF/CeO_2, NiF/CeO_2/Light, NiF/Ag/CeO_2, and NiF/Ag/CeO_2/Light were 530 mV, 410 mV, 330 mV, 280 mV, and 240 mV, respectively, and are shown in Fig. 6b. Fig. 6c illustrates the current density at 0.54 V for NiF, NiF/CeO_2, NiF/CeO_2/Light, NiF/Ag/CeO_2, and NiF/Ag/CeO_2/Light. The values of current densities for NiF, NiF/CeO_2, NiF/CeO_2/Light, NiF/Ag/CeO_2, and NiF/Ag/CeO_2/Light were 10.9 mA cm^{-2}, 21.2 mA cm^{-2}, 25.3 mA cm^{-2}, 35.3 mA cm^{-2}, and 45.7 mA cm^{-2}, respectively (as shown in Fig. 6c). For the HER as well, NiF/Ag/CeO_2 exhibited superior activity to NiF/CeO_2 with an overpotential reduction of 130 mV to achieve a 14.1 mA cm^{-2} enhancement in the current density. Furthermore, the overpotential of NiF/CeO_2 was reduced by 80 mV, and the current density increased by 4.1 mA cm^{-2} on illuminating NiF/CeO_2 with light. Similarly, for NiF/Ag/CeO_2, the overpotential decreased by 40 mV and the current density dramatically increased by 10.4 mA cm^{-2} under light illumination. Fig. 6d presents the Tafel slope (HER) for NiF, NiF/CeO_2, NiF/CeO_2/Light, NiF/Ag/CeO_2, and NiF/Ag/CeO_2/Light. The lowest Tafel slope (HER) was found to be 151 mV dec^{-1} for NiF/Ag/CeO_2 in the presence of light. The reaction mechanism for the HER can be given by the equations:[60]

$$M + H_2O + e^- \rightarrow M\text{–}H_{ad} + OH^-$$

$$2(M\text{–}H_{ad}) \rightarrow 2M + H_2$$

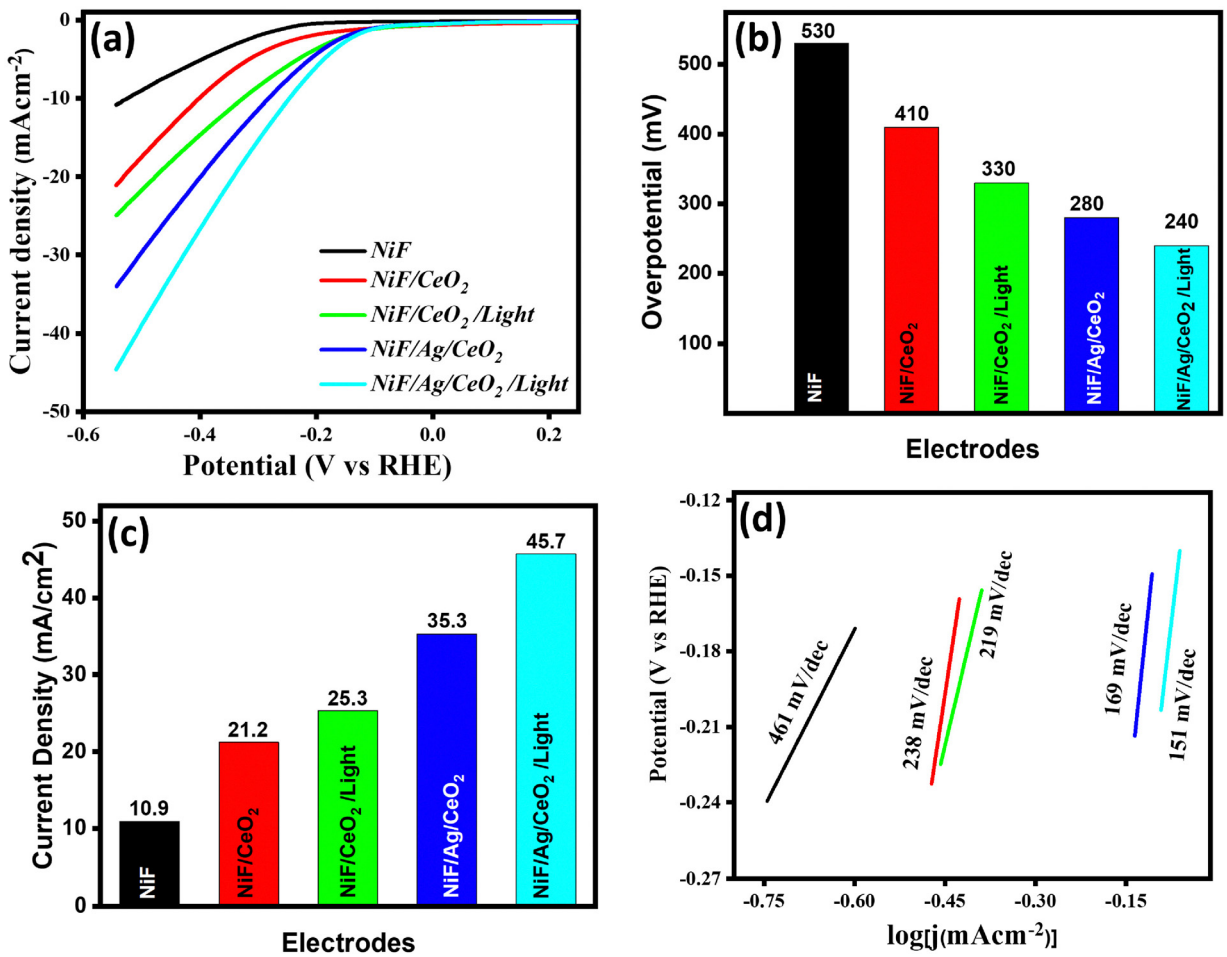

Fig. 6 (a) LSV curves, (b) overpotential (*vs.* RHE) at a current density of 10 mA cm^{-2}, (c) current density at a potential of −0.54 V, and (d) the Tafel slope for the HER of NiF, NiF/CeO_2, NiF/CeO_2/Light, NiF/Ag/CeO_2, and NiF/Ag/CeO_2/Light.

$$2(M\text{–}H_{ad}) + H_2O \rightarrow 2M + 2e^- + H_2 + H_2O$$

The stability of NiF/Ag/CeO_2 in the presence of light was examined using the chronoamperometric study at a constant potential (1.56 V *vs.* RHE) in 1 M KOH solution (see Fig. S8b, ESI†). It was found that NiF/Ag/CeO_2 was stable for a time period of 2 hours.

Proposed mechanism for electrocatalytic water splitting. Based on the results from the characterization techniques and electrocatalytic experiments, a possible mechanism was proposed to understand the electrocatalytic performance of Ag/CeO_2 electrocatalysts. Fig. 7 shows the schematic representation of the photoelectrocatalytic process taking place with the catalyst Ag/CeO_2. Ag/CeO_2 outperforms pristine CeO_2 in the electrocatalytic performance for the OER and HER. Ag/CeO_2 exhibited a 120 mV reduction in the overpotential and a 19.8 mA cm^{-2} increase in the current density compared to pristine CeO_2 for the oxygen evolution reaction. For the hydrogen evolution reaction, Ag/CeO_2 exhibited superior activity to pristine CeO_2 with a 130 mV reduction in overpotential and a 14.1 mA cm^{-2} enhancement in the current density. The reduction in overpotential has been found to be more prominent in Ag/CeO_2 compared to other CeO_2-based catalysts reported previously (Table 3). The distinctively high performance of Ag/CeO_2, especially under light illumination, can be ascribed to the interaction between Ag and CeO_2 generating oxygen vacancies at the metal–support interface. The interaction of Ag and CeO_2 results in (i) a reduction in the band gap of CeO_2, (ii) an improvement in light absorption, (iii) an enhancement in the absorption intensity through the localized surface plasmon resonance (LSPR) effect at the Ag/CeO_2 interface, (iv) an enhancement in the photogenerated electron–hole separation and (v) a delay in electron–hole recombination. The surface oxygen vacancies trap the photogenerated electrons causing a delayed recombination of photogenerated electron and hole pairs. This is supported by the drastic quenching of photoluminescence in Ag/CeO_2. Note that the oxygen evolution reaction occurs in the spin triplet state. Therefore, the presence of spin-polarized electron ensembles can significantly influence the OER, particularly when the reaction cross section involves the transfer of spin-polarized electrons. In the present study, the spin polarization is due to the presence of oxygen vacancies that contribute to the localized spins trapped at the oxygen vacancy sites as has been reported by many researchers.[61]

Table 3 Comparison of overpotential values for the HER and OER at a current density of 10 mA cm^{-2} in 1 M KOH solution, as reported in the literature, for different CeO_2-based catalysts

Catalyst	Reaction	Overpotential (mV) @ 10 mA cm^{-2}	Electrolyte	Ref.
3D-rGO–CeO_2	HER	340	1 M KOH	62
CeO_2/Co $(OH)_2$	HER	317	1 M KOH	63
Ni/ceria	HER	588	1 M KOH	64
Ni/ceria–rGO	HER	208	1 M KOH	52
CeO_2/Ni/NC	HER	320	1 M KOH	65
g-C_3N_4/CeO_2/Fe_3O_4	HER	310	1 M KOH	66
Ag/CeO_2/Light	HER	240	1 M KOH	This work
2.5-RuO_2/CeO_2	OER	460	1 M KOH	67
1-RuO_2/CeO_2	OER	350	1 M KOH	53
5-RuO_2/CeO_2	OER	510	1 M KOH	53
CeO_2/Co@NCH	OER	479	1 M KOH	68
Ag/CeO_2/Light	OER	450	1 M KOH	This work

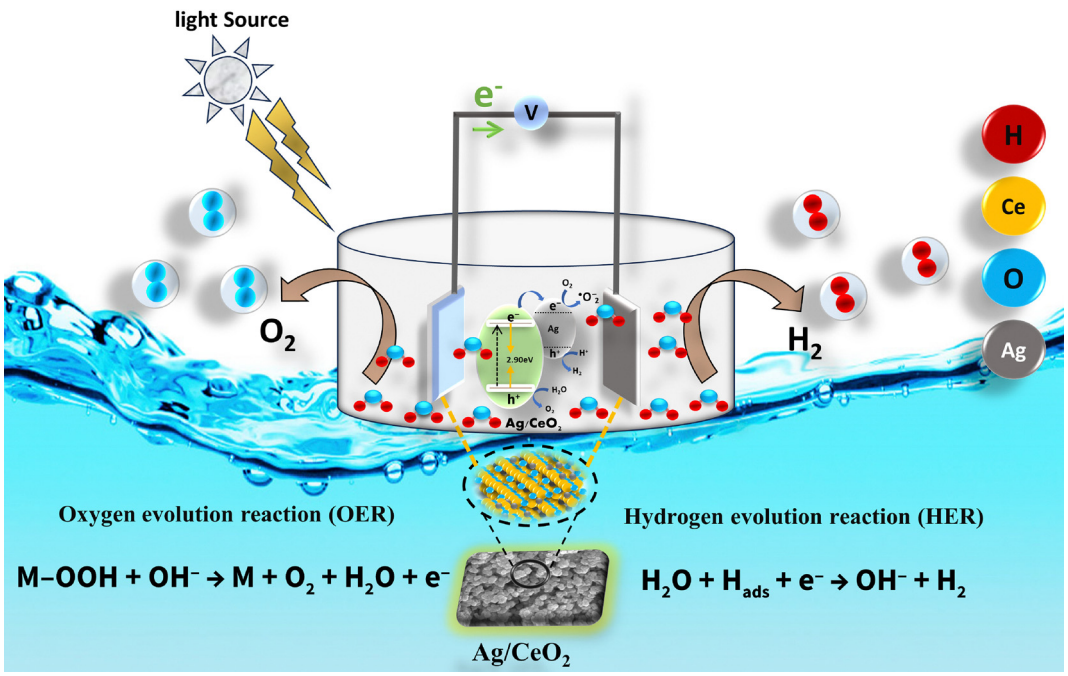

Fig. 7 Mechanism of the electrocatalytic water splitting.

4. Conclusion

In summary, we studied defects induced in ceria that could enhance electrocatalytic water splitting for the oxygen evolution reaction (OER) and hydrogen evolution reaction (HER). Ag/CeO_2 nanocomposites, prepared *via* a facile solvothermal method, exhibit outstanding electrocatalytic performance. The achieved high electrocatalytic activity can be ascribed to the interaction between Ag and CeO_2, which increases the oxygen vacancies at the interface caused by the reduction of Ce^{4+} to Ce^{3+}. The oxygen vacancies at the Ag and CeO_2 interface facilitate photogenerated electron–hole pair separation, resulting in delayed recombination of electron–hole pairs. Raman spectroscopy, X-ray photoelectron spectroscopy, electron paramagnetic resonance spectroscopy and photoluminescence studies confirm the increase in oxygen vacancies in Ag/CeO_2. Besides, the incorporation of Ag onto the surface of CeO_2 reduces the band gap and enhances light absorption, thereby contributing to the enhancement of photoelectrocatalytic activity. Compared to pristine CeO_2, a remarkable enhancement in the electrocatalytic performance of Ag/CeO_2 shows the effect of Ag. The further enhancement of catalytic activity under light illumination reveals the superior photoelectrocatalytic properties of the Ag/CeO_2 composite. A drastic reduction in overpotential and an increase in current density are observed for Ag/CeO_2. For the oxygen evolution reaction, Ag/CeO_2 exhibited a reduction of 120 mV in the overpotential and an increase of 19.8 mA cm^{-2} in the current density compared to CeO_2. For the hydrogen evolution reaction, Ag/CeO_2 exhibited a reduction of 130 mV in the overpotential and an increase of 14.1 mA cm^{-2} in the current density. This work enhances the electrocatalytic performance of Ag/CeO_2 by combining oxygen vacancies with light-assisted catalysis. While many studies focus on either doping or structural modifications, our approach leverages both strategies to significantly increase active site density and improve charge transfer. The light activation further reduces the Tafel slope by 30% in the OER and 11% in the HER, boosting the efficiency of both the OER and HER in Ag/CeO_2. Furthermore, Ag/CeO_2 was found to be stable for a duration of 2 hours under illumination. This synergistic approach can be used for utilizing Ag/CeO_2 as a promising material for photoelectrocatalytic water splitting. Moreover, we believe that the present work not only provides detailed insights into the characterization of defective ceria but also opens up possibilities to develop new ceria-based catalysts for efficient electrocatalytic splitting of water.

Data availability

The data supporting this article have been included as part of the ESI.†

Conflicts of interest

The authors declare no competing financial interests.

Acknowledgements

Ajit Kumar Dhanka thanks the Council of Scientific & Industrial Research (CSIR) and the University Grants Commission (UGC) for the Junior Research Fellowship (JRF)-16-6(119119 Dec. 2018/19). The authors would also like to acknowledge the University Science Instrumentation Centre (USIC), University of Delhi, Special Center for Nanoscience, Jawaharlal Nehru University (JNU), New Delhi, Central Instrumentation Facility (CRF), Jamia Millia Islamia, New Delhi and the Department of Materials Science and Engineering (DMSE), Indian Institute of Technology (IIT) Delhi, New Delhi, India for the characterization facilities. The TEM facilities at the Sophisticated Analytical Instrumentation Facility (SAIF) in All India Institute of Medical Sciences (AIIMS), New Delhi are gratefully acknowledged for the HRTEM measurements.

References

1 D. Pimentel, O. Bailey, P. Kim, E. Mullaney, J. Calabrese, L. Walman and X. Yao, Will limits of the earth's resources control human numbers?, *Environ. Dev. Sustain.*, 1999, **1**, 19–39, DOI: **10.1023/A:1010008112119**.

2 S. Dale (2021). *BP statistical review of world energy*. BP Plc, London, UK, pp. 14–16. **https://www.bp.com/content/dam/bp/business-sites/en/global/corporate/pdfs/energy-economics/statistical-review/bp-stats-review-2021-full-report.pdf**.

3 G. Maggio and G. Cacciola, When will oil, natural gas, and coal peak?, *Fuel*, 2012, **98**, 111–123, DOI: **10.1016/j.fuel.2012.03.021**.

4 F. Umbach, Global energy security and the implications for the EU, *Energy Policy*, 2010, **38**(3), 1229–1240, DOI: **10.1016/j.enpol.2009.01.010**.

5 L. Xu, S. Wu, X. He, H. Wang, D. Deng, J. Wu and H. Li, Interface engineering of anti-perovskite Ni3FeN/VN heterostructure for high-performance rechargeable zinc–air batteries, *Chem. Eng. J.*, 2022, **437**, 135291, DOI: **10.1016/j.cej.2022.135291**.

6 R. M. Navarro, M. A. Pena and J. L. G. Fierro, Hydrogen production reactions from carbon feedstocks: fossil fuels and biomass, *Chem. Rev.*, 2007, **107**(10), 3952–3991, DOI: **10.1021/cr0501994**.

7 J. H. Kim, K. Shin, K. Kawashima, D. H. Youn, J. Lin, T. E. Hong and C. B. Mullins, Enhanced activity promoted by CeOx on a CoOx electrocatalyst for the oxygen evolution reaction, *ACS Catal.*, 2018, **8**(5), 4257–4265, DOI: **10.1021/acscatal.8b00820**.

8 J. X. Feng, S. H. Ye, H. Xu, Y. X. Tong and G. R. Li, Design and synthesis of FeOOH/CeO_2 heterolayered nanotube electrocatalysts for the oxygen evolution reaction, *Adv. Mater.*, 2016, **28**(23), 4698–4703, DOI: **10.1002/adma.201600054**.

9 C. Yang, X. Li, M. Li, G. Liang and Z. Jin, Anchoring oxidation co-catalyst over $CuMn_2O_4$/graphdiyne S-scheme heterojunction to promote eosin-sensitized photocatalytic hydrogen evolution, *Chin. J. Catal.*, 2024, **56**, 88–103, DOI: **10.1016/S1872-2067(23)64563-2**.

10 T. Li, S. Li, Q. Liu, Y. Tian, Y. Zhang, G. Fu and Y. Tang, Hollow Co_3O_4/CeO_2 heterostructures in situ embedded in N-doped carbon nanofibers enable outstanding oxygen evolution, *ACS Sustainable Chem. Eng.*, 2019, **7**(21), 17950–17957, DOI: **10.1021/acssuschemeng.9b04699**.

11 L. Bruno, S. Battiato, M. Scuderi, F. Priolo, A. Terrasi and S. Mirabella, Physical insights into alkaline overall water splitting with NiO micro flowers electrodes with ultra-low amount of Pt catalyst, *Int. J. Hydrogen Energy*, 2022, **47**(80), 33988–33998, DOI: **10.1016/j.ijhydene.2022.08.005**.

12 R. Siavash Moakhar, S. M. Hosseini-Hosseinabad, S. Masudy-Panah, A. Seza, M. Jalali, H. Fallah-Arani and M. Saliba, Photoelectrochemical water-splitting using CuO-based electrodes for hydrogen production: a review, *Adv. Mater.*, 2021, **33**(33), 2007285, DOI: **10.1002/adma.202007285**.

13 D. J. Li, Z. G. Gu, W. Zhang, Y. Kang and J. Zhang, Epitaxial encapsulation of homodispersed CeO_2 in a cobalt–porphyrin network derived thin film for the highly efficient oxygen evolution reaction, *J. Mater. Chem. A*, 2017, **5**(38), 20126–20130, DOI: **10.1039/C7TA06580A**.

14 A. Sivanantham, P. Ganesan and S. Shanmugam, A synergistic effect of Co and CeO_2 in nitrogen-doped carbon nanostructure for the enhanced oxygen electrode activity and stability, *Appl. Catal., B*, 2018, **237**, 1148–1159, DOI: **10.1016/j.apcatb.2017.08.063**.

15 S. Yang and Y. Zhang, Spectroscopic ellipsometry study of Mn doped CeO_2 thin films prepared by radio-frequency magnetron sputtering, *Thin Solid Films*, 2022, **760**, 139516, DOI: **10.1016/j.tsf.2022.139516**.

16 J. Mazloom, F. E. Ghodsi, F. Z. Tepehan, G. G. Tepehan and I. Turhan, Enhanced lithium electrochemical performance and optical properties of CeO_2–SnO_2 nanocomposite thin films by transition metal (TM: Ni, Mn, and Co) doping, *J. Sol-Gel Sci. Technol.*, 2018, **86**, 51–62, DOI: **10.1007/s10971-018-4603-4**.

17 N. V. Bôas, J. B. S. Junior, L. C. Varanda, S. A. S. Machado and M. L. Calegaro, Bismuth and cerium doped cryptomelane-type manganese dioxide nanorods as bifunctional catalysts for rechargeable alkaline metal-air batteries, *Appl. Catal., B*, 2019, **258**, 118014, DOI: **10.1016/j.apcatb.2019.118014**.

18 S. Dai, E. Montero-Lanzuela, A. Tissot, H. G. Baldoví, H. García, S. Navalón and C. Serre, Room temperature design of Ce (IV)-MOFs: from photocatalytic HER and OER to overall water splitting under simulated sunlight irradiation, *Chem. Sci.*, 2023, **14**(13), 3451–3461, DOI: **10.1039/D2SC05161C**.

19 S. Ghosh, S. Pal, M. Biswas, M. Thandavarayan, A. A. Reddy and M. K. Naskar, Dual Active Site Mediated Photocatalytic H_2 Evolution through Water Splitting Using CeO_2/PPy/BFO Double Heterojunction Catalyst, *ACS Appl. Energy Mater.*, 2024, **7**(24), 11453–11465, DOI: **10.1021/acsaem.4c00269**.

20 F. A. C. Oliveira, M. A. Barreiros, A. Haeussler, A. P. Caetano, A. I. Mouquinho, P. M. O. e Silva and S. Abanades, High performance cork-templated ceria for solar thermochemical hydrogen production via two-step water-splitting cycles, *Sustainable Energy Fuels*, 2020, **4**(6), 3077–3089, DOI: **10.1039/D0SE00318B**.

21 P. A. Koyale, S. V. Mulik, J. L. Gunjakar, T. D. Dongale, V. B. Koli, N. B. Mullani and S. D. Delekar, Synergistic enhancement of water-splitting performance using mof-derived ceria-modified g-C_3N_4 nanocomposites: Synthesis, performance evaluation, and stability prediction with machine learning, *Langmuir*, 2024, **40**(26), 13657–13668, DOI: **10.1021/acs.langmuir.4c01336**.

22 M. Orfila, D. Sanz, M. Linares, R. Molina, R. Sanz, J. Marugán and J. Á. Botas, H_2 production by thermochemical water splitting with reticulated porous structures of ceria-based mixed oxide materials, *Int. J. Hydrogen Energy*, 2021, **46**(33), 17458–17471, DOI: **10.1016/j.ijhydene.2020.04.222**.

23 K. Yan, C. Wen, R. Li, B. Zhang, T. Liu, Q. Liu and Z. Zhou, Morphological optimized CeO_2 and Cu-doped CeO_2 nanocrystals for hydrogen production by solar photo-thermochemical water splitting based on surface photoinduced oxygen vacancies, *Appl. Surf. Sci.*, 2023, **636**, 157779, DOI: **10.1016/j.apsusc.2023.157779**.

24 A. Haghighatzadeh, Enhanced third-order optical susceptibility in Ag-doped CeO_2 nanostructures under pulsed Nd-YVO_4 laser, *Opt. Laser Technol.*, 2020, **126**, 106114, DOI: **10.1016/j.optlastec.2020.106114**.

25 X. Miao, H. Yang, J. He, J. Wang and Z. Jin, Adjusting the electronic structure of Keggin-type polyoxometalates to construct S-scheme heterojunction for photocatalytic hydrogen evolution, *Acta Phys.-Chim. Sin.*, 2025, 100051, DOI: **10.1016/j.actphy.2025.100051**.

26 S. Nishimura, D. Mott, A. Takagaki, S. Maenosono and K. Ebitani, Role of base in the formation of silver nanoparticles synthesized using sodium acrylate as a dual reducing and encapsulating agent, *Phys. Chem. Chem. Phys.*, 2011, **13**(20), 9335–9343, DOI: **10.1039/C0CP02985H**.

27 Y. Huang, C. F. Yan, C. Q. Guo, Z. X. Lu, Y. Shi and Z. D. Wang, Synthesis of GO-modified Cu_2O nanosphere and the photocatalytic mechanism of water splitting for hydrogen production, *Int. J. Hydrogen Energy*, 2017, **42**(7), 4007–4016, DOI: **10.1016/j.ijhydene.2016.10.157**.

28 O. L. Pop, A. Mesaros, D. C. Vodnar, R. Suharoschi, F. Tăbăran, L. Mageruşan and C. Socaciu, Cerium oxide nanoparticles and their efficient antibacterial application in vitro against Gram-positive and Gram-negative pathogens, *Nanomaterials*, 2020, **10**(8), 1614, DOI: **10.3390/nano10081614**.

29 K. W. Aga, M. T. Efa and T. T. Beyene, Effects of sulfur doping and temperature on the energy bandgap of ZnO nanoparticles and their antibacterial activities, *ACS Omega*, 2022, **7**(12), 10796–10803, DOI: **10.1021/acsomega.2c00647**.

30 F. Su, P. Li, J. Huang, M. Gu, Z. Liu and Y. Xu, Photocatalytic degradation of organic dye and tetracycline by ternary Ag_2O/AgBr–CeO_2 photocatalyst under visible-light irradiation, *Sci. Rep.*, 2021, **11**(1), 85, DOI: **10.1038/s41598-020-76997-0**.

31 W. Raza, M. M. Haque and M. Muneer, Synthesis of visible light driven ZnO: Characterization and photocatalytic performance, *Appl. Surf. Sci.*, 2014, **322**, 215–224, DOI: **10.1016/j.apsusc.2014.10.067**.

32 L. Zhou, X. Li, Z. Yao, Z. Chen, M. Hong, R. Zhu and J. Zhao, Transition-metal doped ceria microspheres with nanoporous structures for CO oxidation, *Sci. Rep.*, 2016, **6**(1), 23900, DOI: 10.1038/srep23900.

33 N. Agasti and N. K. Kaushik, One pot synthesis of crystalline silver nanoparticles, *Am. J. Nanomater*, 2014, **2**(1), 4–7, DOI: 10.12691/ajn-2-1-2.

34 M. V. Grabchenko, G. V. Mamontov, V. I. Zaikovskii, V. La Parola, L. F. Liotta and O. V. Vodyankina, The role of metal–support interaction in Ag/CeO_2 catalysts for CO and soot oxidation, *Appl. Catal., B*, 2020, **260**, 118148, DOI: 10.1016/j.apcatb.2019.118148.

35 D. Gao, Y. Zhang, Z. Zhou, F. Cai, X. Zhao, W. Huang and X. Bao, Enhancing CO_2 electroreduction with the metal–oxide interface, *J. Am. Chem. Soc.*, 2017, **139**(16), 5652–5655, DOI: 10.1021/jacs.7b00102.

36 Z. Sun, X. Wu, D. Guan, X. Chen, J. Dai, Y. Gu and Z. Shao, One pot-synthesized Ag/Ag-doped CeO_2 nanocomposite with rich and stable 3D interfaces and Ce^{3+} for efficient carbon dioxide electroreduction, *ACS Appl. Mater. Interfaces*, 2021, **13**(50), 59993–60001, DOI: 10.1021/acsami.1c19529.

37 N. Mahmoudi Khatir, Z. Abdul-Malek, A. K. Zak, A. Akbari and F. Sabbagh, Sol–gel grown Fe-doped ZnO nanoparticles: antibacterial and structural behaviors, *J. Sol-Gel Sci. Technol.*, 2016, **78**, 91–98, DOI: 10.1007/s10971-015-3922-y.

38 T. V. M. Sreekanth, P. C. Nagajyothi, P. Muthuraman, G. Enkhtaivan, S. V. P. Vattikuti, C. O. Tettey and K. Yoo, Ultra-sonication-assisted silver nanoparticles using Panax ginseng root extract and their anti-cancer and antiviral activities, *J. Photochem. Photobiol., B*, 2018, **188**, 6–11, DOI: 10.1016/j.jphotobiol.2018.08.013.

39 C. Schilling, A. Hofmann, C. Hess and M. V. Ganduglia-Pirovano, Raman spectra of polycrystalline CeO_2: a density functional theory study, *J. Phys. Chem. C*, 2017, **121**(38), 20834–20849, DOI: 10.1021/acs.jpcc.7b06643.

40 N. Agasti, M. A. Astle, G. A. Rance, J. Alves Fernandes, J. Dupont and A. N. Khlobystov, Cerium oxide nanoparticles inside carbon nanoreactors for selective allylic oxidation of cyclohexene, *Nano Lett.*, 2020, **20**(2), 1161–1171, DOI: 10.1021/acs.nanolett.9b04579.

41 C. Akdogan, B. Gökçal, M. Polat, K. Hamaloğlu, C. Kip and A. Tuncel, Porous, oxygen vacancy enhanced CeO_{2-x} microspheres with efficient enzyme-mimetic and photothermal properties, *ACS Sustainable Chem. Eng.*, 2022, **10**, 9492–9505, DOI: 10.1021/acssuschemeng.2c01981.

42 R. Bhargava, J. Shah, S. Khan and R. K. Kotnala, Hydroelectric cell based on a cerium oxide-decorated reduced graphene oxide (CeO_2–rG) nanocomposite generates green electricity by room-temperature water splitting, *Energy Fuels*, 2020, **34**(10), 13067–13078, DOI: 10.1021/acs.energyfuels.0c02192.

43 Z. Wu, M. Li, J. Howe, H. M. Meyer III and S. H. Overbury, Probing defect sites on CeO_2 nanocrystals with well-defined surface planes by Raman spectroscopy and O_2 adsorption, *Langmuir*, 2010, **26**(21), 16595–16606, DOI: 10.1021/la101723w.

44 W. Cai, Y. Shi, Y. Zhao, M. Chen, Q. Zhong and Y. Bu, The solvent-driven formation of multi-morphological Ag–CeO_2 plasmonic photocatalysts with enhanced visible-light photocatalytic reduction of CO_2, *RSC Adv.*, 2018, **8**(71), 40731–40739, DOI: 10.1039/C8RA08938H.

45 A. L. Cámara, V. C. Corberán, A. Martínez-Arias, L. Barrio, R. Si, J. C. Hanson and J. A. Rodriguez, Novel manganese-promoted inverse CeO_2/CuO catalyst: In situ characterization and activity for the water-gas shift reaction, *Catal. Today*, 2020, **339**, 24–31, DOI: 10.1016/j.cattod.2019.01.014.

46 M. M. Khan, S. A. Ansari, D. Pradhan, D. H. Han, J. Lee and M. H. Cho, Defect-induced band gap narrowed CeO_2 nanostructures for visible light activities, *Ind. Eng. Chem. Res.*, 2014, **53**(23), 9754–9763, DOI: 10.1021/ie500986n.

47 H. Moreno, G. L. Domingues, M. D. Assis, P. P. Ortega, V. R. Mastelaro, M. A. Ramirez and A. Z. Simões, The relationship between photoluminescence emissions and photocatalytic activity of CeO_2 nanocrystals, *Inorg. Chem.*, 2023, **62**(10), 4291–4303, DOI: 10.1021/acs.inorgchem.2c04411.

48 W. Li, S. Xie, M. Li, X. Ouyang, G. Cui, X. Lu and Y. Tong, CdS/CeOx heterostructured nanowires for photocatalytic hydrogen production, *J. Mater. Chem. A*, 2013, **1**(13), 4190–4193, DOI: 10.1039/C3TA10394C.

49 B. Choudhury, P. Chetri and A. Choudhury, Oxygen defects and formation of Ce^{3+} affecting the photocatalytic performance of CeO_2 nanoparticles, *RSC Adv.*, 2014, **4**(9), 4663–4671, DOI: 10.1039/C3RA44603D.

50 X. J. Wen, C. G. Niu, L. Zhang, C. Liang and G. M. Zeng, A novel Ag_2O/CeO_2 heterojunction photocatalysts for photocatalytic degradation of enrofloxacin: possible degradation pathways, mineralization activity and an in-depth mechanism insight, *Appl. Catal., B*, 2018, **221**, 701–714, DOI: 10.1016/j.apcatb.2017.09.060.

51 J. Chen, S. Shen, P. Wu and L. Guo, Nitrogen-doped CeOx nanoparticles modified graphitic carbon nitride for enhanced photocatalytic hydrogen production, *Green Chem.*, 2015, **17**(1), 509–517, DOI: 10.1039/c4gc01683a.

52 P. Dutta, S. Pal, M. S. Seehra, Y. Shi, E. M. Eyring and R. D. Ernst, Concentration of Ce^{3+} and oxygen vacancies in cerium oxide nanoparticles, *Chem. Mater.*, 2006, **18**(21), 5144–5146, DOI: 10.1021/cm061580n.

53 T. Zheng, S. Chen, J. Qin, F. Yang, J. Shi, Y. Hu and Q. He, Pd/CeO_2 Interface with Abundant Oxygen Vacancies for Alkaline Hydrogen Evolution/Oxidation Reaction, *ACS Appl. Nano Mater.*, 2024, 7(2024), 19502–19513, DOI: 10.1021/acsanm.4c03414.

54 N. Wang, W. Qian, W. Chu and F. Wei, Crystal-plane effect of nanoscale CeO_2 on the catalytic performance of Ni/CeO_2 catalysts for methane dry reforming, *Catal. Sci. Technol.*, 2016, **6**(10), 3594–3605, DOI: 10.1039/C5CY01790D.

55 L. Wang, Y. Yu, H. He, Y. Zhang, X. Qin and B. Wang, Oxygen vacancy clusters essential for the catalytic activity of CeO_2 nanocubes for o-xylene oxidation, *Sci. Rep.*, 2017, 7(1), 1–11, DOI: 10.1038/s41598-017-13178-6.

56 J. Li, F. Liu and Y. Li, Fabrication of an Ag/Ag_2 MoO_4 plasmonic photocatalyst with enhanced photocatalytic

performance for the degradation of ciprofloxacin, *New J. Chem.*, 2018, **42**(14), 12054–12061, DOI: **10.1039/C8NJ02327A**.

57 N. T. Suen, S. F. Hung, Q. Quan, N. Zhang, Y. J. Xu and H. M. Chen, Electrocatalysis for the oxygen evolution reaction: recent development and future perspectives, *Chem. Soc. Rev.*, 2017, **46**(2), 337–365, DOI: **10.1039/C6CS00328A**.

58 X. Wang, Y. Li, X. Guo and Z. Jin, In situ synthesis of Ag/Ag_2O on CeO_2 for boosting electron transfer in photocatalytic hydrogen production, *J. Phys. Chem. C*, 2022, **126**(31), 13015–13024, DOI: **10.1021/acs.jpcc.2c03411**.

59 P. A. Koyale and S. D. Delekar, A review on practical aspects of CeO_2 and its composites for photoelectrochemical water splitting, *Int. J. Hydrogen Energy*, 2024, **51**, 515–530, DOI: **10.1016/j.ijhydene.2023.06.251**.

60 J. Yu, G. Li, H. Liu, L. Zeng, L. Zhao, J. Jia and Y. Hu, Electrochemical flocculation integrated hydrogen evolution reaction of Fe@ N-doped carbon nanotubes on iron foam for ultralow voltage electrolysis in neutral media, *Adv. Sci.*, 2019, **6**(18), 1901458, DOI: **10.1002/advs.201901458**.

61 K. Ackland and J. M. D. Coey, Room temperature magnetism in CeO_2-A review, *Phys. Rep.*, 2018, **746**, 1–39, DOI: **10.1016/j.physrep.2018.04.002**.

62 M. Liu, Z. Ji, X. Shen, H. Zhou, J. Zhu, X. Xie and G. Zhu, An Electrocatalyst for a Hydrogen Evolution Reaction in an Alkaline Medium: Three-Dimensional Graphene Supported CeO_2 Hollow Microspheres, *Eur. J. Inorg. Chem.*, 2018, 3952–3959, DOI: **10.1002/ejic.201800757**.

63 M. C. Sung, G. H. Lee and D. W. Kim, CeO_2/$Co(OH)_2$ hybrid electrocatalysts for efficient hydrogen and oxygen evolution reaction, *J. Alloys Compd.*, 2019, **800**, 450–455, DOI: **10.1016/j.jallcom.2019.06.047**.

64 M. Zhiani and S. Kamali, Synergistic effect of ceria on the structure and hydrogen evolution activity of nickel nanoparticles grown on reduced graphene oxide, *J. Mater. Chem. A*, 2017, **5**(17), 8108–8116, DOI: **10.1039/C7TA00146K**.

65 L. Tian, H. Liu, B. Zhang, Y. Liu, S. Lv, L. Pang and J. Li, Ni and CeO_2 nanoparticles anchored on cicada-wing-like nitrogen-doped porous carbon as bifunctional catalysts for water splitting, *ACS Appl. Nano Mater.*, 2021, **5**(1), 1252–1262, DOI: **10.1021/acsanm.1c03850**.

66 D. Xiang, Z. Qin, Y. Gan, X. Luo, X. Li, L. Hu and S. Jiao, Interfacial charge density modulation by coupling CeO_2 with dual-phase NiS/Ni_3S_2 to accelerate alkaline water splitting, *Mater. Today Chem.*, 2023, **34**, 101791, DOI: **10.1016/j.mtchem.2023.101791**.

67 S. M. Galani, A. Mondal, D. N. Srivastava and A. B. Panda, Development of RuO_2/CeO_2 heterostructure as an efficient OER electrocatalyst for alkaline water splitting, *Int. J. Hydrogen Energy*, 2020, **45**(37), 18635–18644, DOI: **10.1016/j.ijhydene.2019.08.026**.

68 A. K. Mishra, J. Willoughby, S. L. Estes, K. C. Kohler and K. S. Brinkman, Impact of morphology and oxygen vacancy content in Ni, Fe co-doped ceria for efficient electrocatalyst based water splitting, *Nanoscale Adv.*, 2024, **6**(18), 4672–4682, DOI: **10.1039/D4NA00500G**.